Enhancement of the irreversibility line in YBa$_2$Cu$_3$O$_{6.95}$ single crystals patterned by heavy ion lithography

F. Laviano,[1] R. Xie,[2,3] E. Mezzetti,[1] and W. K. Kwok[3]

[1]*Department of Physics, Politecnico di Torino, Corso Duca degli Abruzzi 24, 10128 Torino, Italy*
and Istituto Nazionale di Fisica Nucleare Sezione di Torino, Via Pietro Giuria 1, 10125 Torino, Italy
[2]*Department of Physics, University of Notre Dame, Notre Dame, Indiana 46556, USA*
[3]*Materials Science Division, Argonne National Laboratory, 9700 South Cass Avenue, Argonne, Illinois 60439, USA*

High purity, detwinned YBa$_2$Cu$_3$O$_{7-x}$ single crystals were locally irradiated with a stripe pattern using a microcollimated 250 MeV Au ion beam to a dose matching field of B_Φ=4 T. Electron microscopy measurements of the cross section of the irradiated crystal indicate the presence of nanometer columnar defects confined to a surface layer (blind holes) and an ensemble of ancillary defects in the bulk of the crystal. We present systematic studies of the effects of blind hole structures and of ancillary defects using quantitative magneto-optical imaging with a Bi:yttrium iron garnet indicator film. We observed a local reduction in the superconducting critical temperature near the surface layer where the blind holes were formed, due to the high irradiation fluence. The difference in the critical temperature between the surface layer and the bulk of the irradiated stripe zones enabled us to isolate and estimate the enhancement of the local vortex pinning due solely to the ancillary defects induced by the irradiation. We find that the blind holes with the additive contribution of the ancillary defects produce a pronounced upward shift in the irreversibility line and stronger vortex pinning with respect to the unirradiated stripe regions both at low and at high temperatures.

I. INTRODUCTION

Soon after the discovery of high temperature superconductors (HTSCs), it was recognized that irradiation with high energy heavy ions (HEHIs) was an effective method to enhance the vortex pinning capabilities of the perovskite oxide based HTSC.[1] The HEHI irradiation produces nanometric scale defects with a well-defined morphology for HEHI energy, exceeding the threshold of 20 MeV/amu for HTSC YBa$_2$Cu$_3$O$_{7-x}$ (YBCO).[1] In this case, the ion impact results in the quasicontinuous amorphization of the material due to the interaction with electrons along the HEHI path, creating columnar defects (CDs).[1] The effect of CDs in the HTSC compounds is being intensively studied both for fundamental science and for applications.

The vortex pinning of CDs extending through the entire thickness of the sample was demonstrated to be close to the maximum attainable pinning capabilities of HTSC compounds due to the geometrical matching of the vortex structure with the CDs and the onset of a Bose glass phase.[2–4] When the energy of the HEHI is low enough, such that the CDs do not extend over the entire thickness of the crystal, the ancillary defects are created depending on the amount of the local energy release along the ion path. It was earlier reported that truncated CDs (named hereafter as *blind holes*) and implantation of the HEHI into the HTSC materials also produce vortex pinning enhancements, especially at high temperatures and at high magnetic fields.[5–7]

In this paper, we present a quantitative magneto-optical (QMO) imaging study of the magnetic field distribution in a high quality YBCO single crystal, which was locally irradiated in an alternating stripe pattern in order to simultaneously compare the intrinsic and the irradiation induced magnetic responses in a single sample. The cross section of the irradiated region was imaged by field emission scanning electron microscopy (FESEM) in order to elucidate the induced defect landscape. We found three regions characterized by different defect morphologies: a surface layer with blind holes (BHs), an intermediate defected region ending at the implantation depth of the ions, and an additional defected region beyond the implantation depth but terminating inside the bulk of the crystal. Because of the high density of irradiation defects induced in the sample, we observed a lowering of the local superconducting critical temperature, T_c, in the surface layer containing the BHs. The lower T_c ($=T_c^{\mathrm{BH}}$) enabled us to separate, in the QMO measurements, the effect of the ancillary defect ensemble created by the HEHI irradiation from the BHs and to thoroughly investigate their pinning behavior.

II. EXPERIMENT DETAILS

The high purity YBCO single crystals were grown by the flux growth method and detwinned by applying uniaxial pressure.[8] The critical temperature T_c of these optimally doped crystals exceeds 93 K. The single domain samples for QMO measurements were cleaved into platelets. The sample length, width, and thickness are $300 \times 200 \times 23$ μm^3, respectively.

For 250 MeV Au ion irradiation, SRIM© code simulations,[9,10] presented in Fig. 1, indicate that BHs are created in a top layer of roughly 5 μm from the crystal surface, at least when the HEHI energy is above the threshold indicated in Fig. 1(a).[7,11] In addition, a cascade of ancillary defects propagates down to the implantation length of about 13 μm, as shown in Fig. 1(b). Defect straggling could be observed in the ancillary defect region, as indicated in Fig. 1(c). In irradiated melt-textured YBCO samples, it was
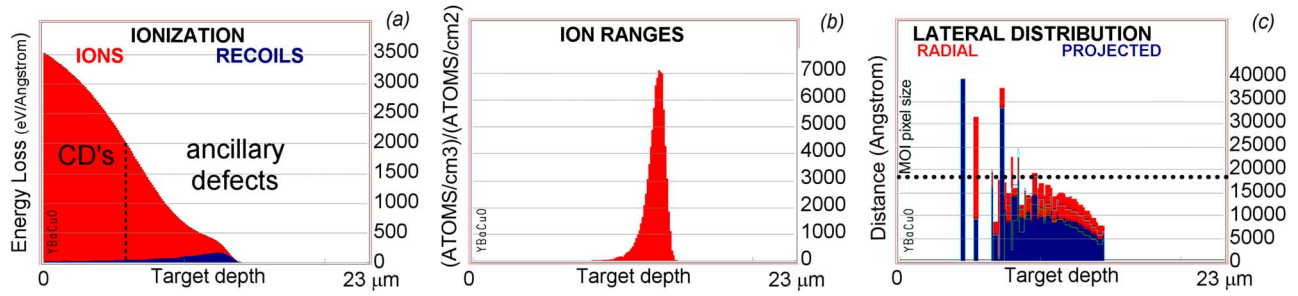
FIG. 1. (Color online) SRIM© simulation for the irradiation and the material parameters considered here. (a) Ionization energy loss plot indicating the energy threshold for the formation of straight CDs. (b) Ion range plot with the implantation depth and straggle. (c) Lateral distribution plot showing the splaying of the defects when the ions start to scatter and form ancillary defects.

verified that the implantation depth predicted by the SRIM simulation was accurate to within 4%.[12] In high purity perovskite single crystals, some deviations are expected due to the ion channeling and the secondary emission phenomena.[13]

The irradiation was performed at the INFN Tandem facilities with ^{197}Au ions accelerated to 250 MeV. The HEHI beam was microcollimated by means of a stainless steel mask (150 μm thick) with a slit aperture of 30 μm.[14] The "stripe" irradiation pattern is sketched in Fig. 2(a). The optical images of both faces of the crystal presented in Figs. 2(b) and 4(c) confirm that the HEHI beam was stopped well inside the crystal bulk.

The FESEM measurements of the crystal cross section were performed in order to image the defect landscape induced in the crystal bulk [top side of the crystal, as indicated by the arrow in Fig. 2(b)]. The high quality of the crystal enabled us to directly visualize the defect distribution throughout the thickness, as shown in Fig. 3(a). Three main defected regions can be distinguished in Fig. 3(a), in addition to a remaining undisturbed part of the crystal at the bottom. Straight CDs are observed in a top layer of about 6.1 μm, as shown in Fig. 3(b), which abruptly terminate at a rough boundary. Two additional interfaces separate the other defected areas: the implantation layer with a peculiar boundary [Fig. 3(c)] and a straight crack separating the bottom undisturbed crystal layer. We think that this crack was due to a post-irradiation stress release mechanism between regions

with different strain contributions. Remarkably, we found an additional defected region beyond the implantation depth, presumably generated by the secondary emission processes occurring due to the HEHI impacts at the implantation threshold layer. These additional defects constitute nearly 40% of the thickness of the ancillary defected region apart from the BH layer.

The visualization of the magnetic pattern was performed using the QMO technique with Bi:yttrium iron garnet indicator films[15] (see for details Ref. 16). Special care was taken when manually positioning the indicator film over the crystal in order to minimize the indicator-to-sample distance (i.e., maximizing magnetic and spatial resolutions, as discussed in detail below) and to improve the optical response of the indicator itself.

In the entire set of QMO frames presented here, the darker regions correspond to low or null magnetic fields along the axis perpendicular to the sample surface and the bright contrast corresponds to high magnetic flux density. The light intensity maps were carefully calibrated with an iterative procedure,[17] taking into account the full 3D magnetic field distribution at the measurement plane. This procedure is based on the deconvolution of the Biot–Savart law in Fourier space and on the calculation of the in-plane field distribution generated by the current density of the sample. The in-plane field values are used for the correction of the measured light intensity values (see Ref. 17 for details). Al-
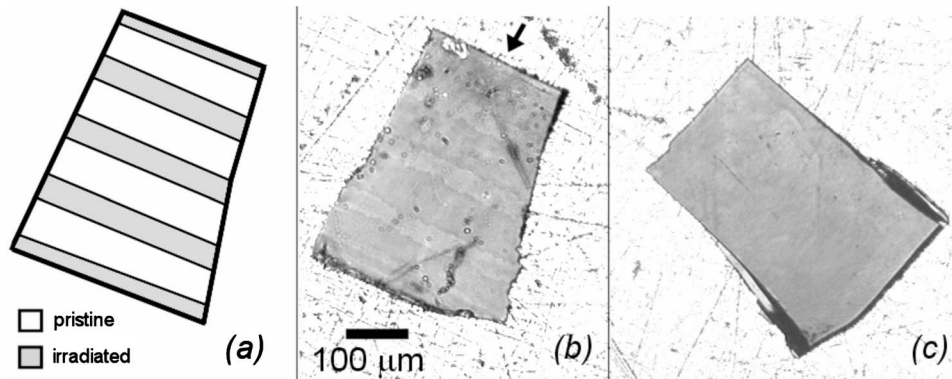

FIG. 2. (a) Schematic of the alternating stripe irradiation pattern consisting of irradiated and unirradiated strips. The irradiated strips are 30 μm wide. (b) Polarized light optical image of the irradiated crystal face. The irradiated areas are clearly visible with a dark contrast. The arrow points to the crystal section that was measured by FESEM. (c) The bottom crystal face does not display any sign of the irradiation damage.
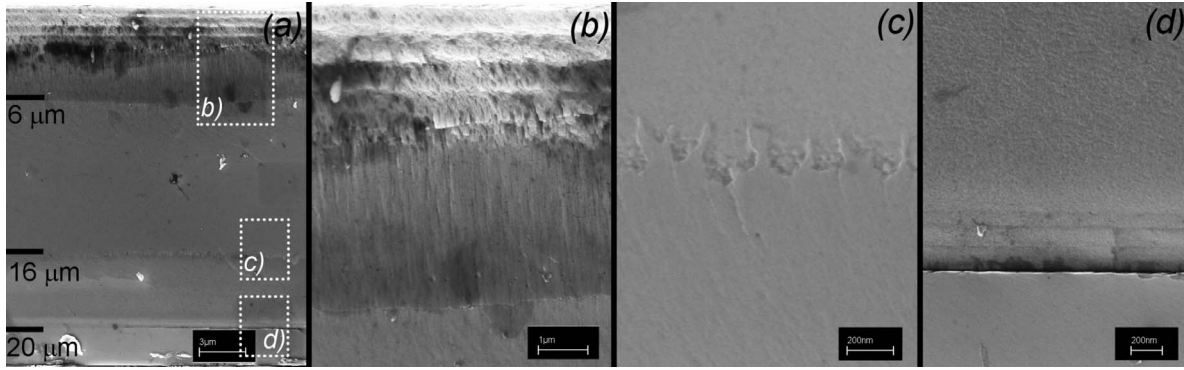
FIG. 3. (a) The complete crystal cross section measured by FESEM (irradiated surface on top). (b) The higher magnification of the first 8 μm layer where the columnar defects are directly observed. The linear correlation of the columnar defects abruptly stops at about 6 μm. The interface (marked by the dark to light contrast on the bottom) is speculated to be generated by the strain between the top amorphized layer and a less damaged part before the HEHI implantation. (c) The HEHI implantation region. Several rounded amorphized areas are observed. (d) Pointlike and other defects generated by the secondary emission (near the implantation region) are present down to 20 μm where a straight crack is observed. This crack is generated by the same strain relaxation mechanism speculated above. Note that the bottom layer (about 3 μm) seems to be completely free of defects, demonstrating the very high quality of the unirradiated YBCO crystal.

though the crystal is relatively thick for the magnetic field applied along the crystal c axis, the current distribution is mainly determined by the in-plane components that are 40 times larger than the perpendicular one in this sample.[18] Hence, the deconvolution scheme actually evaluates the local current density that corresponds, at each pixel, to the sum of the current loop planes throughout the crystal thickness. However, since the thickness (23 μm) is larger than the pixel size (1.8 μm), the quantitative current density values used for estimating the critical current ratio between the irradiated and the unirradiated zones are unambiguously determined and averaged[19] over an area of 25×25 μm^2.

III. RESULTS AND DISCUSSIONS

A. Low temperature vortex behavior

The magnetic field and supercurrent distributions are shown in Figs. 4(a) and 4(b), and in Figs. 4(c) and 4(d), respectively, for the crystal irradiated with a HEHI fluence of 1.93×10^{11} ions cm^{-2} (corresponding to a dose matching field of $B_\Phi = 4$ T), at $T = 4.15$ K. The sample was first zero field cooled (ZFC) and then a sequence of increasing magnetic fields were applied perpendicular to the sample surface (the QMO frames in Fig. 4 correspond to $\mu_0 H = 150$ mT). Figures 4(a) and 4(c) correspond to the irradiated face of the crystal, and Figs. 4(b) and 4(d) to the rear face. For both crystal faces, the magnetic field and supercurrent distributions show an inhomogeneous critical state, similar to the case considered in Ref. 20, that closely follows the stripe irradiation pattern portrayed in Fig. 2(a). The striking similarity of the macroscopic critical state patterns demonstrates that the vortex pinning strength of the ancillary defects induced in the bulk is comparable to that of the BHs. The pinning strengths of the irradiated sections are enhanced by a factor of about 1.8 for both faces at low temperature.

Since we are taking into account the convolution of the magnetic pattern on the length scale of the crystal thickness, it is remarkable to note that any possible contribution of the

defect straggling in the irradiated part of the crystal can only contribute to the vortex pinning of the ancillary defect ensemble due to the enhanced pinning from the mixing of correlated, splayed, and pointlike defects at the relatively low vortex densities used in our experiment.[21–23] On the other hand, since the upper bound for the lateral defect diffusion in the unirradiated areas can be estimated from the FESEM measurement to be less than 4 μm,[24] we can also disregard the lateral diffusion when measuring with an optical magnification corresponding to about 2 μm per pixel.
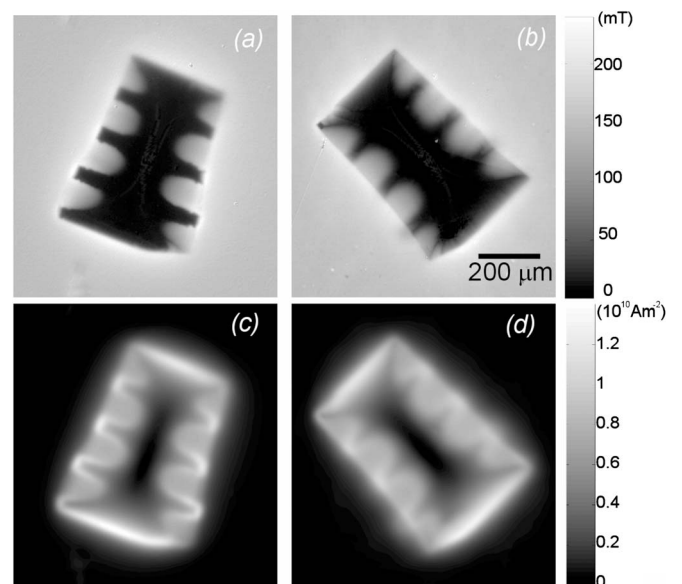

FIG. 4. Magnetic field distribution is shown in (a) for the irradiated face of the crystal and in (b) for the opposite face, while (c) and (d) show supercurrent distributions for both crystal faces, at $T = 4.15$ K and $\mu_0 H = 150$ mT. The crystal displays a vortex pinning enhancement of about 180% in the irradiated zones. Note that the quantitative current density values are appropriately evaluated when averaged over 25×25 μm^2 areas due to the thickness of the sample (23 μm).
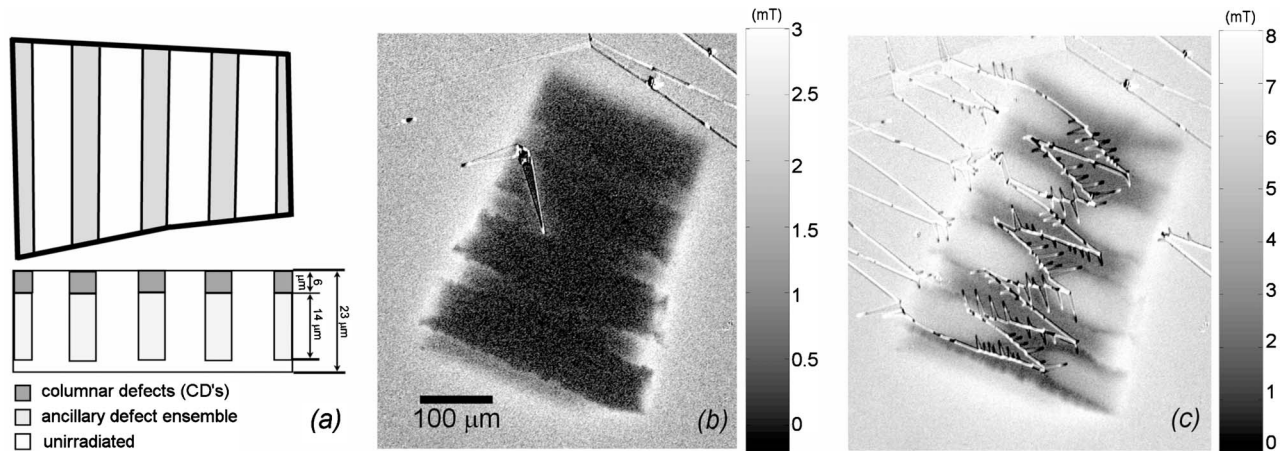
FIG. 5. (a) The schematic view of the crystal; in-plane view on the top and cross-section view on the bottom. The surface regions where BHs were formed display a decrease in T_c, leading to the normal state at $T > 86$ K. (b) The magnetic field distribution at $T = 88$ K with $\mu_0 H = 1.5$ mT after ZFC. The shallow bright contrast in the irradiated zones indicates the increase by means of a stainless steeling effective gap between the QMO indicator film and the superconducting part of the sample that generates the supercurrent loops. In particular, this effect is clearly seen over the top and bottom irradiated regions. The loss of QMO contrast is absent for $T < 86$ K. (c) The magnetic field distribution at $T = 88$ K with $\mu_0 H = 6$ mT. The vortices start to penetrate the crystal and it is clearly shown that the pinning capabilities of the irradiated areas are enhanced with respect to the unirradiated regions. The triangular pattern is due to the domain walls in the QMO indicator film.

The microscopic deviations in the magnetic field pattern of the two faces can be observed at the interfaces between the irradiated and unirradiated zones. In particular, the high contrast in the QMO signal, delineating flux focusing along the interfaces,[20] is visible in Fig. 4(a) but not in Fig. 4(b). This occurs only if the observed magnetic flux structure is confined to the top irradiated layer and the characteristic flux structure size is much smaller than the *effective* distance to the measurement plane, i.e., tens of nanometers in Fig. 4(a) but several microns in Fig. 4(b). In the latter figure, the indicator film, which defines the measurement plane, is placed on the opposite side with respect to the irradiated face where the current source plane generating such a feature is located. Moreover, in Fig. 4(b), a blurred contrast is also visible just outside the wider bottom edge. Since some edge tails are thinner than the crystal bulk [see the optical image in Fig. 2(c)], it turns out that the faces near these tails are further away from the indicator film in Fig. 4(b) while they are in better contact with the rest of the flat crystal surface in Fig. 4(a). The flux structure is resolved in this case because the characteristic source size is comparable or larger than the gap between the indicator film and the crystal's surface. Generally, a large gap between the indicator film and the current source plane causes loss of both the signal contrast and the spatial resolution.[25,26] The ability to detect and to distinguish the stray field generated by sources at different distances from the measurement plane is important for the following analysis.

B. High temperature vortex behavior

For the HEHI fluence considered here, the T_c^{BH} of the irradiated sections of the top surface where the BHs are formed is expected to be depressed with respect to the unirradiated regions since such high irradiation fluences induce large strain in the interstitial regions around the amorphous ion tracks;[27] in particular, for uniform Pb ion irradiation of YBCO with $B_\Phi = 4$ T, it was reported that the critical temperature is reduced to 86 K.[28] The local T_c reduction was also observed for the microcollimated high fluence Au irradiation at the same energy on YBCO films.[29]

The investigation of the high temperature regime, $T > T_c^{BH}$, enables the estimation of the additive vortex pinning contribution of the ancillary correlated defects separately. Remarkably for $T > 86$ K ($= T_c^{BH}$), the superconducting transition of the surface layer where there are BHs [roughly $200 \times 30 \times 6$ μm^3 for each zone, as sketched in the cross-section scheme of Fig. 4(a)] was indeed observed from the QMO measurements.

The first evidence of reduced T_c comes from the loss of the local QMO contrast in the irradiated stripe sections. This is related to an abrupt increase in the effective distance between the supercurrent source and the measurement plane (indicator film), as discussed above. In this way, the QMO provides a depth profile of the supercurrent source. Figure 5(b) shows the magnetic pattern when a magnetic field is initially applied just after ZFC. A shallow magnetic contrast is visible over the irradiated strips, apparently indicating that the vortices initially entered into these regions. On the other hand, Fig. 5(c) shows the magnetic field distribution corresponding to a succession of applied magnetic fields and clearly indicates that, when vortices start entering the bulk, they are pinned stronger in the irradiated channels, as observed from the largely reduced vortex entry rate. Since we did not observe any reduction in the surface barriers[30] in the irradiated regions up to T_c^{BH}, we conclude that the bright contrast over the irradiated regions observed in Fig. 5(b) can only be due to the local increase in the *effective* separation between the indicator film and the supercurrent planes of a few microns.[31] Another evidence of local transition of the
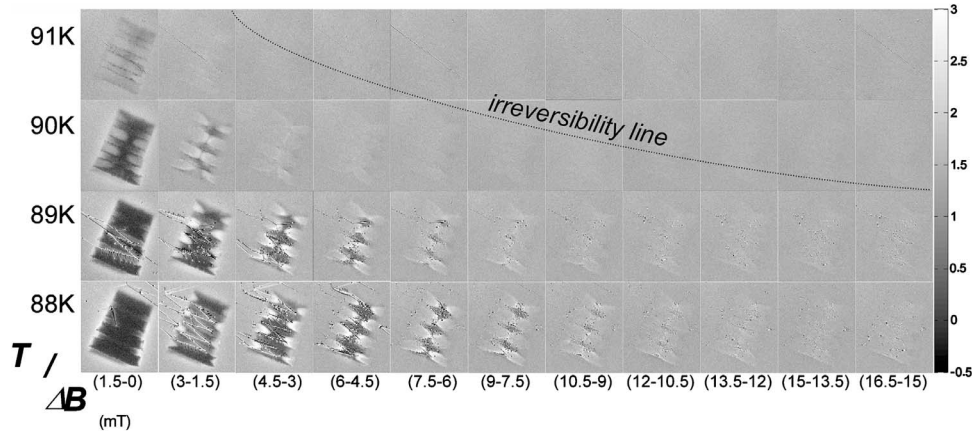
FIG. 6. (B-T) phase diagram constructed from the QMO measurements of the $\Delta B / \Delta H$ distribution. Each frame corresponds to the difference between two consecutive measurements made with the applied magnetic field ($\mu_0 H$) values indicated in parentheses on the horizontal axis. The darker contrast represents a better screening with respect to the bright regions where vortices are diffusing and accumulating. The saw tooth pattern is the ferromagnetic domain-wall structure of the indicator film. The dashed line represents an average irreversibility signal for the entire crystal (it corresponds to the disappearance of the magnetic field gradient contrast). Starting from the left-bottom frame, the pinning capabilities of the irradiated regions are clearly enhanced up to $T=90$ K. At $T=91$ K, the vortex pinning due to the thickness modulation at interfaces between the unirradiated and irradiated parts seems to be the main irreversible mechanism present in the system.

irradiated surface layers was obtained from observing and registering a dynamical instability of the trapped magnetic flux caused by the local current redistribution[32] when the sample is rapidly warmed above 86 K.

A subset of QMO frames in the temperature range 88 K $\leq T < 92$ K is presented in Fig. 6 in such a way as to construct the (B-T) phase diagram of the crystal for $T > T_c^{\mathrm{BH}}$. The subsequent frames were subtracted from each other in order to display the difference in the local magnetic response of the crystal with the increasing applied magnetic fields (i.e., a quantity that is related to the local permeability). The dashed line is the irreversibility line, corresponding to the loss of the nonlinear and irreversible signal for the entire crystal (e.g., as it can be measured with the bulk magnetization or other similar techniques). The effect of the ancillary defects becomes particularly evident because the irreversible signal of the unirradiated part is vanishing much faster with the increasing applied field or temperature. Namely, a vanishing supercurrent is inferred from the decay of the magnetic field gradient up to a constant magnetic profile (i.e., vanishing irreversible signal), corresponding to the same grayscale level as the area outside the sample (e.g., for the unirradiated parts, the irreversible signal is lost in the first frame at 91 K, in the fourth frame from the left for 90 K, and in the eighth frame from the left for 89 K, etc.).

Moreover, the magnetic field gradient in the unirradiated parts is always weaker than in the irradiated channels (whose contrast is always darker than the other parts), i.e., the critical current in the irradiated parts is always larger than in the unirradiated regions.

Remarkably, at $T=91$ K, some screening capability is observed near the boundaries between the irradiated and unir-

radiated parts of the crystal (tiny and irregular dark stripes in the first QMO frame at 91 K). Since the surface layer of the crystal where the BHs are formed is in the normal state at this temperature, we assume that this additive pinning contribution comes from the local modulation of the *effective* crystal thickness where the supercurrent flows and provides additional evidence for the local transition of the top layer where BHs are present.

IV. CONCLUSIONS

In summary, we demonstrated that the HEHI irradiation, at energies that are insufficient to induce straight CDs traversing the entire thickness of the crystal, instead produces an ancillary defect ensemble that enhances the vortex pinning with respect to the unirradiated material at all temperatures. The critical temperature of the crystal is slightly depressed on the surface layer where BHs are formed due to the HEHI irradiation. We showed that the ancillary defects in the bulk of the crystal are efficient vortex pinners over a wider temperature range than CDs extending the entire crystal thickness.

[1] B. Hensel, B. Roas, S. Henke, R. Hopfengartner, M. Lippert, J. P. Strobel, M. Vildic, G. Saemann-Ischenko, and S. Klaumunzer, Phys. Rev. B **42**, 4135 (1990); L. Civale, A. D. Marwick, T. K. Worthington, M. A. Kirk, J. R. Thompson, L. Krusin-Elbaum, Y. Sun, J. R. Clem, and F. Holtzberg, Phys. Rev. Lett. **67**, 648 (1991); M. Konczykowski, F. Rullier-Albenque, E. R. Yacoby, A. Shaulov, Y. Yeshurun, and P. Lejay, Physica C **185-189**, 2347 (1991); R. C. Budhani, M. Suenaga, and S. H. Liou, Phys. Rev. Lett. **69**, 3816 (1992).

[2] I. F. Lyuksyutov, Europhys. Lett. **20**, 273 (1992).

[3] D. R. Nelson and V. M. Vinokur, Phys. Rev. B **48**, 13060 (1993).

[4] J. Figueras, T. Puig, X. Obradors, W. K. Kwok, L. Paulius, G. W. Crabtree, and G. Deutscher, Nat. Phys. **2**, 402 (2006).

[5] E. Mezzetti, R. Cherubini, R. Gerbaldo, G. Ghigo, L. Gozzelino, and B. Minetti, Nuovo Cimento D **18**, 1099 (1996).

[6] E. Mezzetti, R. Gerbaldo, G. Ghigo, L. Gozzelino, and L. Gherardi, Phys. Rev. B **59**, 3890 (1999); D. Botta, A. Chiodoni, R. Gerbaldo, G. Ghigo, L. Gozzelino, F. Laviano, B. Minetti, and E. Mezzetti, Physica C **408-410**, 32 (2004).

[7] L. Trappeniers, J. Vanacken, L. Weckhuysen, K. Rosseel, A. Yu. Didyk, I. N. Goncharov, L. I. Leonyuk, W. Boon, F. Herlach, V. V. Moshchalkov, and Y. Bruynseraede, Physica C **313**, 1 (1999).

[8] U. Welp, M. Grimsditch, H. You, W. K. Kwok, M. M. Fang, G. W. Crabtree, and J. Z. Liu, Physica C **161**, 1 (1989).

[9] J. F. Ziegler, J. P. Biersack, and U. Littmark, *The Stopping and Range of Ions in Solids* (Pergamon, New York, 1985), Vol. 1, pp. 1–321.

[10] SRIM 2006 is available at http://www.srim.org.

[11] G. Ghigo, R. Gerbaldo, L. Gozzelino, E. Mezzetti, B. Minetti, and A. Wisniewski, J. Supercond. **10**, 541 (1997).

[12] L. Gozzelino, R. Gerbaldo, G. Ghigo, E. Mezzetti, B. Minetti, P. Schatzle, G. Krabbes, E. Carlino, and G. Cuttone, Philos. Mag. B **80**, 1015 (2000).

[13] M. C. Frischherz, M. A. Kirk, J. P. Zhang, and H. W. Weber, Philos. Mag. A **67**, 1347 (1993).

[14] A. Rovelli, A. Amato, D. Botta, A. Chiodoni, R. Gerbaldo, G. Ghigo, L. Gozzelino, F. Laviano, B. Minetti, and E. Mezzetti, Nucl. Instrum. Methods Phys. Res. B **240**, 842 (2005); E. Mezzetti, D. Botta, A. Chiodoni, R. Gerbaldo, G. Ghigo, L. Gozzelino, F. Laviano, B. Minetti, A. Rovelli, A. Amato, and R. Cherubini, in *Advances in Cryogenic Engineering Materials*, edited by U. Balachandran (American Institute of Physics, New York, 2006), Vol. 52.

[15] L. A. Dorosinskii, M. V. Indenbom, V. I. Nikitenko, Yu A. Ossip'yan, A. A. Polyanskii, and V. K. Vlasko-Vlasov, Physica C **203**, 149 (1992).

[16] Ch. Jooss, J. Albrecht, H. Kuhn, S. Leonhardt, and H. Kronmuller, Rep. Prog. Phys. **65**, 651 (2002).

[17] F. Laviano, D. Botta, A. Chiodoni, R. Gerbaldo, G. Ghigo, L. Gozzelino, S. Zannella, and E. Mezzetti, Supercond. Sci. Technol. **16**, 71 (2003).

[18] Taking into account the aspect ratio (1/8) and the out-of-plane/in-plane supercurrent anisotropy ratio of YBCO (1/5).

[19] This is done in Fourier space by setting the cutoff spatial frequency equal or larger than the sample thickness.

[20] Th. Schuster, H. Kuhn, E. H. Brandt, M. V. Indenbom, M. Klaser, G. Muller-Vogt, H.-U. Habermeier, H. Kronmuller, and A. Forkl, Phys. Rev. B **52**, 10375 (1995).

[21] G. P. Mikitik and E. H. Brandt, Phys. Rev. B **62**, 6800 (2000).

[22] A. V. Silhanek, L. Civale, and M. A. Avila, Phys. Rev. B **65**, 174525 (2002).

[23] F. Laviano, D. Botta, A. Chiodoni, R. Gerbaldo, G. Ghigo, L. Gozzelino, and E. Mezzetti, Phys. Rev. B **68**, 014507 (2003).

[24] Taking into account an isotropic distribution of the induced defects.

[25] L. Dorosinskii, H. Bocuk, U. Topal, and C. Birlikseven, Supercond. Sci. Technol. **14**, 839 (2001).

[26] The intensity of the magnetic moment measured at the indicator plane indeed exponentially depends on the distance between the indicator and the source plane (in k space). See Eq. (4.8) in Ref. 17.

[27] Y. Yan and M. A. Kirk, Phys. Rev. B **57**, 6152 (1998).

[28] R. J. Olsson, W. K. Kwok, L. M. Paulius, A. M. Petrean, D. J. Hofman, and G. W. Crabtree, Phys. Rev. B **65**, 104520 (2002).

[29] F. Laviano, R. Gerbaldo, G. Ghigo, L. Gozzelino, B. Minetti, and E. Mezzetti, Appl. Phys. Lett. **89**, 082514 (2006).

[30] M. Konczykowski, L. I. Burlachkov, Y. Yeshurun, and F. Holtzberg, Phys. Rev. B **43**, 13707 (1991).

[31] The physical distance between the indicator film and the sample was estimated by the iterative deconvolution method to be of the order of 100 nm.

[32] Real-time videos can be found at http://www2.polito.it/ricerca/superconductivity/MO/Instability_videos